

Revised surface abundances of R Coronae Borealis stars

Gajendra Pandey, B. P. Hema, and Arumalla B. S. Reddy

Indian Institute of Astrophysics, Bangalore, Karnataka, 560034, India

pandey@iiap.res.in; hemabp.phy@gmail.com; balasudhakara.reddy@iiap.res.in

ABSTRACT

Surface abundances of 14 (11 majority class and 3 minority class) R Coronae Borealis stars (RCBs) along with the final flash object, V4334 Sgr (Sakurai’s object) are revised based on their carbon abundances measured from the observed C_2 bands; note that the earlier reported abundances were derived using an assumed carbon abundance due to the well known “carbon problem”. The hot RCB MV Sgr is not subject to a carbon problem; it is remarkable to note that MV Sgr’s carbon abundance lies in the range that is measured for the majority and minority class RCBs. The revised iron abundances for the RCBs are in the range $\log \epsilon(\text{Fe})=3.8$ to $\log \epsilon(\text{Fe})=5.8$ with the minority class RCB V854 Cen at lower end and the majority class RCB R CrB at the higher end of this range. Indications are that the revised RCBs’ metallicity range is roughly consistent with the metal poor population contained within the bulge. The revised abundances of RCBs are then compared with extreme helium stars (EHes), the hotter relatives of RCBs. Clear differences are observed between RCBs and EHes in their metallicity distribution, carbon abundances, and the abundance trends observed for the key elements. These abundances are further discussed in the light of their formation scenarios.

Subject headings: stars: atmospheres – stars: abundances – stars: chemically peculiar – stars: evolution

1. Introduction

R Coronae Borealis stars (RCBs) are F- and G-type supergiants with carbon rich and hydrogen deficient atmospheres. In these stars, the measured hydrogen-to-helium ratio by

number is $\leq 10^{-2}$ that stands in contrast to a solar-type star’s H/He of 10. The surface abundances of hydrogen poor stars are measured relative to helium, the most abundant element in their atmospheres. The next most abundant element in their atmospheres is carbon followed by nitrogen and oxygen, and the rest are the trace elements including hydrogen. Spectroscopic determination of carbon-to-helium ratio is not possible from the observed optical spectra of RCBs – photospheric neutral helium lines are not expected for their effective temperatures and neutral carbon lines are roughly of the same strength across the range in their effective temperature unlike the lines from other elements, for example, iron. Hence, a carbon-to-helium ratio of 1.0% by number is assumed to derive the surface abundances of RCBs. This assumption comes from the extreme helium stars (EHes), seemingly the close relatives of RCBs, having C/He ratios of about 1.0%.

Of about 128 known Galactic RCBs (Tisserand et al. 2020) including the 11 new RCBs from Palomar Gattini IR (PGIR) survey (Karambelkar et al. 2021), abundance analyses are available for only about 22 – a very small sample indeed (Asplund et al. 2000; Rao & Lambert 2008; Hema et al. 2017) to draw conclusions on their origin and evolution as a group.

In this paper, the dependence of the derived surface abundances on the adopted model atmosphere’s C/He ratios are discussed. Here, we report the revised surface abundances based on the derived carbon abundance, that is the C/He ratio, from the observed C_2 bands in an RCB’s spectrum (Hema et al. 2012b, 2017). These new abundances are further compared with the abundances of EHes, and are then discussed in the light of their formation scenarios.

2. Abundances

2.1. Fundamentals

In an observed star’s spectrum, the strength of an absorption line is always defined as the depth of the line with respect to the continuum. Thus, the strength of an absorption line (weak) of an element X is controlled by the line absorption coefficient relative to the continuum absorption coefficient. In the case of a normal (H-rich) star’s optical spectrum with effective temperature in the range similar to RCBs, the continuum and the line absorption coefficients are proportional to the number density of H and X atoms, respectively. Then, the number density ratio X/H is what dictates the line strength and is normally expressed as the abundance of an element X. X/H can be further stated in terms of the mass fraction $Z(X)$ by assuming He/H ratio of 0.1 that comes from hot normal stars and is an unobservable quantity for cool stars.

In the optical, theory and observations of RCBs’ atmospheres suggest that photoionization of C I is the dominant source of continuum opacity in their line-forming layers (Asplund et al. 1997a). The near constant equivalent widths of weak C I lines observed in their optical spectra from one star to another is notable (see Figure 1 of Rao & Lambert (1996)). Therefore, the measure of abundance of an element X in RCBs is the ratio X/C. However, it is crucial to express the measured abundance $A(X) = X/C$ in terms of the more fundamental quantity: the mass fraction $Z(X)$. Which calls for the determination or assumption of the C/He ratio, since helium is expected to be the most abundant element in their atmospheres. The mass fraction, $Z(X)$ is given as

$$Z(X) = \frac{\mu_X X}{\mu_H H + \mu_{He} He + \mu_C C + \dots} = \frac{\mu_X X}{(\sum \mu_I I)} \quad (1)$$

where μ_I is the atomic mass of element I. The denominator which represents summation over all the elements is a conserved quantity through the different stages of nuclear burning. Assuming helium to be the most abundant ingredient, the equation 1 in terms of the measured abundance $A(X) = X/C$ is redefined as

$$Z(X) = \frac{\mu_X A(X)}{H/C + 4He/C + 12 + \dots \mu_I I/C} \quad (2)$$

Due to hydrogen being very poor in these stars, H/C relative to He/C is very very small and can be ignored like other trace elements from the denominator, then the above equation reduces to,

$$Z(X) \simeq \frac{\mu_X}{4} \frac{C}{He} A(X) \quad (3)$$

The C/He is spectroscopically determined for 14 RCBs from their observed C₂ bands (Hema et al. 2012b, 2017), and also the abundance of any element X for a hydrogen-deficient star like RCBs, can be directly measured spectroscopically i.e., $A(X) = X/C$.

The derived abundances are normalised based on the convention that $\log \epsilon(X) = \log(X/H) + 12.0$ to a scale in which $\log \sum \mu_I \epsilon(I) = 12.15$, where 12.15 is determined from solar abundances with He/H $\simeq 0.1$. Based on this normalisation convention, from equation 3, the helium abundance $\log \epsilon(He)$ is about 11.54 for a C/He ≤ 0.01 . The abundance of an element X can be expressed in terms of mass fraction $Z(X)$ or number fraction X/He, and these two quantities are related as shown in equation 3. Here, stars’ derived abundances are given in $\log \epsilon(X)$ and the notation $[X]$ represents abundance of X in a star relative to that in the Sun or log number relative to solar.

2.2. RCB stars

The surface abundances of about 22 RCBs are available in literature as mentioned in Section 1. These abundances were derived by adopting a C/He of 1%, or that is by assuming the carbon abundance $\log \epsilon(\text{C}) = 9.54$. Note that, from equation 3, the derived abundances depend on the adopted C/He ratio but the abundance ratios do not. For example, $\log \epsilon(\text{X}/\text{Fe})$ is independent of the adopted C/He ratio. Four RCBs: VZ Sgr, V CrA, V854 Cen, and V3795 Sgr, are classified as minority class RCBs that show relatively lower Fe abundances and higher Si/Fe and S/Fe ratios than the majority class RCBs (Asplund et al. 2000).

In this paper, the surface abundances of 14 RCBs (11 majority class and 3 minority class) including their fluorine abundances (Pandey et al. 2008; Hema et al. 2017) are revised using their spectroscopically determined carbon abundances from observed C_2 bands (Hema et al. 2012b, 2017). The revised abundances for all the elements except helium, can be obtained by a simple scaling down of the derived abundances (for an assumed C/He) by a factor, that is the difference between the assumed and the determined $\log \epsilon(\text{C})$. The factor, ΔC , by which the derived abundance (for an assumed C/He) was scaled down is given in Table 1. Before presenting their revised abundances, we comment on the two known facts related to their derived carbon abundances.

First, the predicted strengths of the C I lines are stronger than the observed. That means, the carbon abundance derived using state-of-the-art H-deficient model atmospheres (Asplund et al. 1997a) is about 0.6 dex reduced from that chosen for constructing the model atmosphere. Asplund et al. (2000) gave a name the “carbon problem” to this mismatch. A more severe “carbon problem” was found for the observed [C I] lines (Pandey et al. 2004a). Resolutions to the “carbon problem” were provided by crafting state-of-the-art model atmospheres by hand (Asplund et al. 2000; Pandey et al. 2004a). Pandey et al. (2004a)’s hand crafted model atmospheres bring the predicted strengths of C I and [C I] lines in agreement with the observations. However, this holds for all the carbon abundances, from $\log \epsilon(\text{C})=8.5$ (C/He=0.1%) through $\log \epsilon(\text{C})=10.5$ (C/He=10%), adopted for constructing the model atmosphere. This implies that predicted strengths of C I and [C I] lines are insensitive to the carbon abundance.

Second, the carbon abundances derived from observed C_2 bands are independent of the adopted model’s carbon abundance and this is described as the C_2 carbon problem (Hema et al. 2012b). The solution to the so called C_2 carbon problem may lie in the modification of the model atmosphere’s temperature structure as shown by Pandey et al. (2004a). However, it is yet to be shown that real atmospheres have flatter temperature gradients, as suggested by Asplund et al. (2000), than the present state-of-the-art model atmospheres. Therefore, it cannot be ruled out that the carbon abundances derived from C_2 bands are the

real measure of carbon abundances in these stars. In principle, the carbon abundances measured from C₂ Swan bands and that assumed for the model atmosphere can be equated for a particular choice of C/He that varies from star to star. This removes the carbon problem for C₂ bands. Also, as expected for carbon rich stars, the carbon abundance derived from C₂ bands is correlated with the O abundance (Hema et al. 2012b). (Note that the carbon abundance from C I lines is not well correlated with the O abundance). Hence, we adopt the carbon abundance or the C/He ratio derived from C₂ bands (Hema et al. 2012b, 2017) for revising the RCBs’ abundances. The revised abundances, deduced from the above described procedure, are given in Table 1.

3. The Galactic positions and orbits

It is crucial to know whether RCBs and their apparent relatives, the EHes are members of the Milky Way’s bulge (the central regions) or the halo (the outer regions). To confirm their membership, the distances and orbits of these stars have been determined. The distances to these stars were determined using the Parallax measurements made by the Gaia satellite. Note that, the Gaia mission measures a star’s proper motion and radial velocity (RV) with unprecedented precision. The RV measurements of several RCBs and EHes also come from Asplund et al. (2000); Hema et al. (2012b); Pandey et al. (2001); Jeffery et al. (1987); Pandey et al. (1996) and the best or an average value is adopted based on our judgement. The orbits around the Galaxy have been estimated in combination with their distances and velocities. The required data for calculating the orbits for the following RCBs: GU Sgr, UX Ant, R CrB, RS Tel, SU Tau, V482 Cyg, FH Sct, V2552 Oph, V532 Oph, ASAS-RCB-10, VZ Sgr, and MV Sgr (the hot RCB) were available. For the following EHes: LSS 3184, BD−9°4395, LS IV+6°002, LSE 78, LSS 4357, V1920 Cyg, LSS 99, HD 124448, BD+10°2179, PV Tel, FQ Aqr, LS IV−1° 002, BD−1°3438, LS IV−14° 109, and LSS 3378, data were available for calculating the orbits. The initial conditions for the computation of Galactic orbits of stars are their presently observed positions and velocities with respect to the galactocentric reference frame. Adopting the solar motion $(U, V, W)_{\odot} = (10.0, 5.2, 7.2)$ km s^{−1} from Dehnen & Binney (1998), the local standard of rest (LSR) velocities of stars U_{LSR} , V_{LSR} , W_{LSR} and their errors σ_U , σ_V , σ_W are calculated with the method of Johnson & Soderblom (1987). The LSR velocities are then corrected to the Galactic standard of rest (GSR) by adopting the LSR rotation velocity of 220 km s^{−1} (Kerr & Lynden-Bell 1986) at the galactocentric distance of the Sun of 8.5 kpc. The celestial positions (α, δ, l, b) , parallaxes (π) , and absolute proper motions $(\mu_{\alpha} \cos \delta, \mu_{\delta})$ are adopted from the Gaia Early Data Release 3 (Gaia Collaboration et al. 2016, 2020), while the RV measurements are taken from the published sources as mentioned above. Adopting the measured Galactic spatial positions and

velocities, we studied the dynamics of stars under the influence of a multicomponent, static, axisymmetric Galactic gravitational potential model of Flynn et al. (1996). The relevant code adopted here for the integration of stellar orbits was used previously in the analysis of kinematics and orbits of a large sample of open clusters (Wu et al. 2009; Reddy et al. 2016). Starting with a star’s current position and velocity components referenced to the Galactic standard of rest, the trajectory of the star was followed backward in time over a period of 5 Gyr to ensure that each star could complete sufficient galactic orbits so that the averaged orbital parameters can be determined with fair certainty.

The analysed RCBs with accurate kinematics have tightly bound orbits, placing them in the inner regions of the Milky Way of radius less than or about 6.0 kpc and z_{max} about 3.0 kpc, the exceptions being UX Ant, V482 Cyg, SU Tau, and R CrB. In contrast, the analysed EHes with accurate kinematics have orbits extending beyond the regions of the Milky Way of radius more than 6.0 kpc, the exceptions being LSS 4357, LSIV–1° 002, and LSIV–14° 109. Including MV Sgr, we note that about five analysed RCBs with accurate kinematics have tightly bound orbits and z_{max} similar to the most metal-poor, $\log \epsilon(\text{Fe}) \sim 3.5$, star SMSS J181609.62–333218.7 whose orbit is entirely contained within the bulge (Howes et al. 2015). The revised metallicity range for the analysed RCBs is $\log \epsilon(\text{Fe}) = 3.8$ through $\log \epsilon(\text{Fe}) = 5.8$ (see Table 1), and the revised metallicities are fairly consistent with their estimated orbits and location in the Galaxy.

4. RCB and EHe stars: surface compositions

The RCBs’ revised surface composition, based on the carbon abundances derived from the observed C₂ bands, provide new evidences for their formation history. We discuss by comparing the revised surface compositions of RCBs with EHes that are considered to be their relatives having higher effective temperatures. The surface composition of EHes including the hot RCB star DY Cen are from Jeffery & Heber (1992); Drilling et al. (1998); Jeffery (1998); Jeffery et al. (1998); Pandey et al. (2001, 2004b, 2006); Pandey (2006); Pandey & Reddy (2006); Pandey & Lambert (2011); Pandey et al. (2014); Pandey & Lambert (2017); Jeffery (2017); Bhowmick et al. (2020). The principal objective is to seek out similarities, differences, and trends if any.

4.1. The C/He ratios

The carbon abundances for the RCBs are in the range $\log \epsilon(\text{C})=7.7$ to $\log \epsilon(\text{C})=8.8$ that is the C/He ratios are in the range 0.02 to 0.2 per cent including the three minority class RCB stars. In contrast, the C/He ratios of the EHes are in the range 0.3 to 1.0 per cent with three exceptions. The three exceptions are V652 Her, HD 144941, and GALEX J184559.8–413827, having very low C/He ratios ~ 0.003 per cent. The two hot RCBs, MV Sgr (Jeffery et al. 1988) and DY Cen have C/He ratios of 0.02 and 1.0 per cent, respectively. However, recent study of Jeffery et al. (2020) indicates that DY Cen’s evolutionary history involves a very late thermal pulse due to its very rapid evolution, non-negligible surface hydrogen and high surface strontium.

The hot RCB MV Sgr is not subject to a carbon problem like EHes. It is remarkable to note that MV Sgr’s C/He ratio lies in the range that is derived for the majority and minority class RCBs.

4.2. Iron: the initial metallicity

The revised iron abundances for the RCBs are in the range $\log \epsilon(\text{Fe})=3.8$ to $\log \epsilon(\text{Fe})=5.8$ with the minority class RCB V854 Cen at lower end and the majority class RCB R CrB at the higher end of this range (see Table 1). On the contrary, the iron abundances for the EHes are in the range $\log \epsilon(\text{Fe})=5.4$ to $\log \epsilon(\text{Fe})=7.2$. As discussed in Section 3, EHes are broadly placed in the outer regions of the Milky Way than the RCBs. Indications are that the RCBs’ metallicity range is roughly consistent with the metal poor population contained within the bulge (Howes et al. 2015).

Hydrogen- and helium-burning products are clearly observed in the atmospheres of RCBs and EHes. Their derived effective temperatures and surface gravities suggest that they are evolved low mass stars. Hence, no synthesis of α - and Fe-peak elements occurs in the course of their evolution. The α - and Fe-peak elements remain unaltered in their atmospheres by providing us the initial metallicity to these stars; here α -peak elements usually refer to α -capture elements heavier than neon.

4.3. Hydrogen

The hydrogen abundance of majority class RCB stars show no obvious trend with the iron abundance or the metal abundance. However, it is notable that two minority class RCBs

V CrA and V854 Cen with relatively lower Fe abundance have hydrogen abundance higher than the majority class RCBs. The third minority class RCB VZ Sgr is like the majority class RCBs (See Figure 1: bottom left panel). For a comparison, EHe stars are shown in Figure 1: bottom right panel. Note the relatively higher hydrogen abundances of DY Cen and the three very low C/He EHe stars.

4.4. The CNO abundances

The majority class RCBs' carbon abundances are a function of their Fe abundances but this trend is not very evident for the minority class RCBs (see Figure 1: top left panel). However, abundances for only three minority class RCBs are available and so it is not worth looking for any trends. In contrast for EHes, Figure 1: top right panel clearly demonstrates that carbon abundances are independent of their Fe abundances.

The nitrogen abundances of both RCBs and EHes depend on their Fe abundances (see Figure 2: bottom left panel for RCBs and bottom right panel for EHes). The observed N abundance is the sum of initial CNO as expected. Hence, providing the evidence that helium is produced from hydrogen-burning CNO cycle that converts most of the initial C and O to N.

If all of initial C and O is converted to N, then the CNO cycle processed material should be N enriched with C and O depleted. The observed C and O abundances for both RCBs and EHes are not depleted suggesting that these are products of helium-burning via triple- α and α -capture on ^{14}N and ^{12}C . The three exceptions that show depleted C and O are the very low C/He or C-poor EHe stars (see Figure 1: top left panel for RCBs and top right panel for EHes, and Figure 2: top left panel for RCBs and top right panel for EHes).

4.5. Fluorine

The fluorine abundances of the majority and minority class RCBs suggest a mild trend with their Fe abundances and F/Fe in these stars is highly enriched when compared to the solar F/Fe ratio. Most of the EHes have enhanced F like RCBs but show no trend with their Fe abundances unlike RCBs. See Figure 3: bottom left panel for RCBs and bottom right panel for EHes, for F versus Fe trends.

4.6. Neon

For EHes, the neon abundances like N abundances are enhanced and show a trend with their Fe abundances except for the five cool EHes whose Ne abundances are not corrected for the non-LTE effects. Application of the non-LTE effects brings the Ne abundances of cool EHes in line with the hot EHes (Pandey & Lambert 2011). The dependence of the Ne abundance with the Fe abundance suggest that the observed Ne in EHes is essentially ^{22}Ne and is produced from two successive α -captures on ^{14}N . Note that the revised Ne abundances are available only for two RCBs. The Ne versus Fe trends are shown in Figure 3: top left panel for RCBs and top right panel for EHes.

4.7. Sodium to zinc

The EHe and RCB abundances of sodium, aluminium, magnesium, silicon, sulphur, calcium, titanium, chromium, manganese, nickel, and zinc scale well with the iron abundances. For RCBs, Al, Mg, Si, S, Ca, Ti, Ni and Zn broadly vary in concert with Fe, as expected. Similar correlations are seen for EHes with additions of Cr and Mn. This clearly indicates that the EHe as well as RCB star's Fe abundance is the representative of initial metallicity. Abundances of phosphorus, argon, chromium, and manganese are not available for RCBs, but in EHes it is worth considering the observed abundances of P and Ar that suggest weak correlations with Fe. The X versus Fe trends are shown in Figures 4, 5, 6, 7, 8, 9, and 10. The left and the right panels show RCBs and EHes, respectively. Note the variation of minority class RCBs with respect to the majority class RCBs.

4.8. Yttrium, zirconium, and barium: heavy elements

For majority class RCBs, the revised abundances of Y and Zr show insignificant enhancements. However, the minority class RCBs show a range from insignificant to a maximum enhancement of about 2.0 dex in both Y/Fe and Zr/Fe with respect to the solar Y/Fe and Zr/Fe ratios like the EHes. Barium for majority as well as minority class RCBs shows insignificant enhancement. Note that only three measurements of Ba are available for EHes showing a range from no to a maximum enhancement of about 1.8 dex in Ba/Fe with respect to the solar Ba/Fe ratio. See Figures 10 and 11: the left and the right panels show RCBs and EHes, respectively.

5. Key spectroscopic features

The key features of RCBs are specifically their high $^{12}\text{C}/^{13}\text{C}$ and low $^{16}\text{O}/^{18}\text{O}$ ratios with remarkable F overabundances (Hema et al. 2012b; Clayton et al. 2007; Pandey et al. 2008). $^{12}\text{C}/^{13}\text{C}$ and $^{16}\text{O}/^{18}\text{O}$ ratios are from observed C_2 and CO molecular bands in the spectra of RCBs but these molecular bands are not present in the observed spectra of EHes due to their higher effective temperatures. Nevertheless, fluorine atomic lines are observed in EHes’ as well in RCBs’ spectra and provide the star’s F abundance. The atmospheres of EHes are overabundant in F like RCBs (Pandey 2006; Bhowmick et al. 2020). The processes involving fluorine production in these stars needs to be explored. For this reason, it will be crucial to identify any correlations between fluorine and other elements including any relationship among the abundances of other key elements.

5.1. F versus CNO and Ne

In RCBs, the F abundances suggest mild to no correlation with C abundances. In contrast, EHes’ F abundances are strongly correlated with their C abundances. See Figure 12: the top left and the top right panels show RCBs and EHes, respectively.

F versus N show significant correlation in RCBs unlike in EHes. Figure 13: the top left and the top right panels clearly exhibit these trends for RCBs and EHes, respectively. F versus O and Ne trends are also shown in Figure 14: the left and the right panels are for RCBs and EHes, respectively.

We note that the relationship of F with C and that with N is distinct for RCB and EHe stars. This indicates that, possibly, fluorine is produced from two different processes operating in these stars.

5.2. C and N versus O

C and O abundances suggest linear correlation for both RCBs and EHes. These trends are clearly shown in Figure 12: the bottom left and the bottom right panels are for RCBs and EHes, respectively. The N versus O abundances are also shown in Figure 13: the bottom left and the bottom right panels are for RCBs and EHes, respectively.

6. Double white dwarf mergers and the abundances of key elements

The RCB and EHe stars’ origins and evolutionary connections are not yet understood despite thorough analyses of their spectra. In broad terms, the chemical compositions suggest a hydrogen-deficient atmosphere now composed of material exposed to both H- and He-burning. Following the elimination of several proposals, two principal theories emerged: the “double-degenerate” (DD) model and the “final-flash” (FF) model.

The FF model, refers to a late or final He shell flash in a post-AGB star. In this model (Iben et al. 1983), the ignition of the helium shell in a post-AGB star, say, a cooling white dwarf, results in what is known as a late or very late thermal pulse (Herwig 2001). This converts the star to a H-poor cool luminous star (i.e., an RCB star), which then evolves to hotter effective temperatures at about constant luminosity (i.e., as an EHe star), and finally to the white dwarf cooling track. The attendant nucleosynthesis during and following the He shell flash shows that a H-poor supergiant may result with surface composition characteristic of RCBs and EHes. However, the FF model has failed to account for the key features, particularly, the high $^{12}\text{C}/^{13}\text{C}$ ratios, the low $^{16}\text{O}/^{18}\text{O}$ ratios and anomalous F overabundances observed in these stars (Pandey 2006; Clayton et al. 2007; Pandey et al. 2008; Rao & Lambert 2008; Hema et al. 2012b, 2017). A consensus is now emerging for DD model but a small fraction of H-poor stars may be produced from FF model (Pandey & Lambert 2011) such as the majority RCB XX Cam, and possibly the EHe HD 124448 (Bhowmick et al. 2020) including V4334 Sgr (Sakurai’s object) (Pandey et al. 2008). The surface abundances of V4334 Sgr (Asplund et al. 1997b) are revised based on the measured carbon abundance, that is $\log \epsilon(\text{C}) = 9.7$ (Hema et al. 2012a), from C_2 bands as done for RCBs. For comparison, the revised abundances of V4334 Sgr for the 1996 October spectrum are given in Table 1 .

The DD scenario, proposed by Webbink (1984) and Iben & Tutukov (1984), involves the merger of an He white dwarf with a more massive C-O white dwarf following the decay of their orbit. Other mergers may involve two He white dwarfs. It is clear that the merger product will be H-poor since neither of the white dwarfs contain much hydrogen, and the hydrogen that survives will be mixed substantially with more helium and possibly other material. Recall the extraordinary $^{16}\text{O}/^{18}\text{O}$ ratios in RCBs and/or the remarkable F overabundances in RCBs as well as in EHes. Neither CO+He white dwarf binaries nor He+He white dwarf binaries can account for these exceptional abundances without the ensuing nucleosynthesis during the merger and/or the postmerger phase. Simulations of the merger and postmerger phases with accompanying nucleosynthesis have been attempted for evolution of a white dwarf merger to the RCB phase (Longland et al. 2011; Zhang & Jeffery 2012b,a; Menon et al. 2013, 2019; Zhang et al. 2014; Lauer et al. 2019).

Simulations of He+He white dwarf mergers are limited to Zhang & Jeffery (2012b,a)

and appear to be “in partial agreement” in explaining the observed abundances of RCBs and EHes. Bhowmick et al. (2020) note that F is underpredicted by Zhang & Jeffery (2012a) while minor disagreements between prediction and observation are found for C, N, O, and Ne. In these mergers, the F is synthesized by $^{14}\text{N}(\alpha, \gamma)^{18}\text{F}(p, \alpha)^{15}\text{O}(\alpha, \gamma)^{19}\text{Ne}(\beta^+)^{19}\text{F}$. However, Zhang & Jeffery (2012b) provide the latitude to account for the C-poor V652 Her and HD 144941 (Pandey & Lambert 2017).

Most recent calculations for a CO+He merger are from Crawford et al. (2020). It is clear that surface composition of the merger products are a result of mixing during and/or following the merger. In post-merger objects, the temperature of the helium-burning shell at ignition strongly impacts the yields of CNO-process as well as α -capture isotopes. Hence, Crawford et al. investigate the effects of a range of initial He-burning shell temperatures and include the effects of solar and subsolar metallicities. Their three models that satisfy the maximum criteria in reproducing the observed surface abundances are SOL8.57, SUB8.48, and SUB8.53; SOL and SUB represent models with metallicity solar and one-tenth of solar, respectively, and 8.57, 8.48, and 8.53 are the models’ initial He-burning shell temperatures (K) in common log values. Crawford et al. were able to identify SUB8.48 as the preferred model that is able to remarkably reproduce abundances closest to those of observed RCBs. SUB8.48 is at 10 per cent of solar metallicity with an initial He-burning shell temperature of approximately 3.00×10^8 K; the other closest model SUB8.53 yields higher C, F, and Ne with no significant changes in N and O yields (see Figures 1, 2, and 3). The predicted surface Li abundance ($\log \epsilon(\text{Li})$) is between 0.85 and 2.64 for solar models, while the subsolar models have significantly higher Li abundances, between 3.95 and 6.41. The Crawford et al.’s predicted surface Li can possibly be an upper limit because their reaction network, `mesa_75.net`, as noted by them does not include the crucial reaction $^7\text{Li}(\alpha, \gamma)^{11}\text{B}$. However, inclusion of ^{11}B in the reaction network reduces the predicted surface Li abundance ($\log \epsilon(\text{Li})$) significantly to about -1.5 to 1.0 for one-tenth of solar metallicity white dwarf mergers (Munson et al. 2021).

7. Concluding Remarks

Predictions of CO+He white dwarf mergers are in good agreement with the observed abundances, in particular with the extraordinary overabundance of F (Menon et al. 2013, 2019). Menon et al. (2013) identify that one source of F is in the He-burning shell where $^{13}\text{C}(\alpha, n)^{16}\text{O}$ provides the neutrons to seed the reaction $^{14}\text{N}(n, p)^{14}\text{C}(p, \gamma)^{15}\text{N}(\alpha, \gamma)^{19}\text{F}$. The correlations of F with C and N indicate that plausibly F production in majority class RCBs is via the reaction channel: $^{14}\text{N}(\alpha, \gamma)^{18}\text{F}(p, \alpha)^{15}\text{O}(\alpha, \gamma)^{19}\text{Ne}(\beta^+)^{19}\text{F}$; F abundance depends

on ^{14}N and the available protons (see Section 5.1, and Figures 12 and 13). While in EHes, the dependence of F with C and N suggests that F is produced via the reaction channel: $^{14}\text{N}(n, p)^{14}\text{C}(p, \gamma)^{15}\text{N}(\alpha, \gamma)^{19}\text{F}$; F abundance depends on the available neutrons but on the other hand, ^{13}C which provides neutrons must result from the mixing of protons into a ^{12}C -rich region, where the ^{12}C comes from ^4He (see Section 5.1 and Figures 12 and 13). For example, if F synthesis is via the reaction channel involving neutrons, then the star’s F abundance is expected to be correlated with its ^{12}C abundance. On the contrary, if the reaction involving α -capture on ^{14}N is producing F, then the star’s F abundance is expected to be correlated with its N abundance. Nonetheless, the trends of F with C, N, O, and Ne show that significant helium burning after a double white dwarf merger can account for a majority of the observed abundances (see Section 5.1, and Figures 12, 13, and 14). It is worth noting that the average of observed F abundances is lower by about 1 dex in RCBs than in EHes for stars with common Fe abundance (see Figure 3).

The revised Fe abundances ($\log \epsilon(\text{Fe})$), that is the metallicity, of RCBs are in the range 3.8 through 5.8. These revised metallicities are fairly consistent with their estimated orbits and location in the Galaxy. Recent (Crawford et al. 2020; Munson et al. 2021) and the earlier predictions of CO+He white dwarf mergers do not explore the metallicity range lower than $\log \epsilon(\text{Fe})=6.5$. The revised metallicity range observed for RCB stars is lower than $\log \epsilon(\text{Fe})=6.5$. Hence, predictions for CO+He white dwarf mergers are lacking for the revised lower metallicities of RCB stars. However, an extrapolation of Crawford et al.’s surface abundance predictions to lower metallicities, similar to the revised metallicity range of RCBs, would likely explain the observed carbon abundances from C_2 bands but not all the observed key elemental abundances. The revised C/O ratios that are between 3.0 and 64.0 may possibly be explained; tweaking of several parameters mainly the initial He-burning shell temperature may likely reproduce the RCBs’ revised abundances. Theoretical studies with a larger parameter space, for example including all the key reactions, needs to be explored to explain the revised abundances of RCBs, and this would certainly lead to further refinements in the study of white dwarf mergers.

We thank the referee for the constructive comments. GP is grateful to Kameswara Rao, David Lambert and Simon Jeffery for introducing him to the topic of H-poor stars, and for all their help.

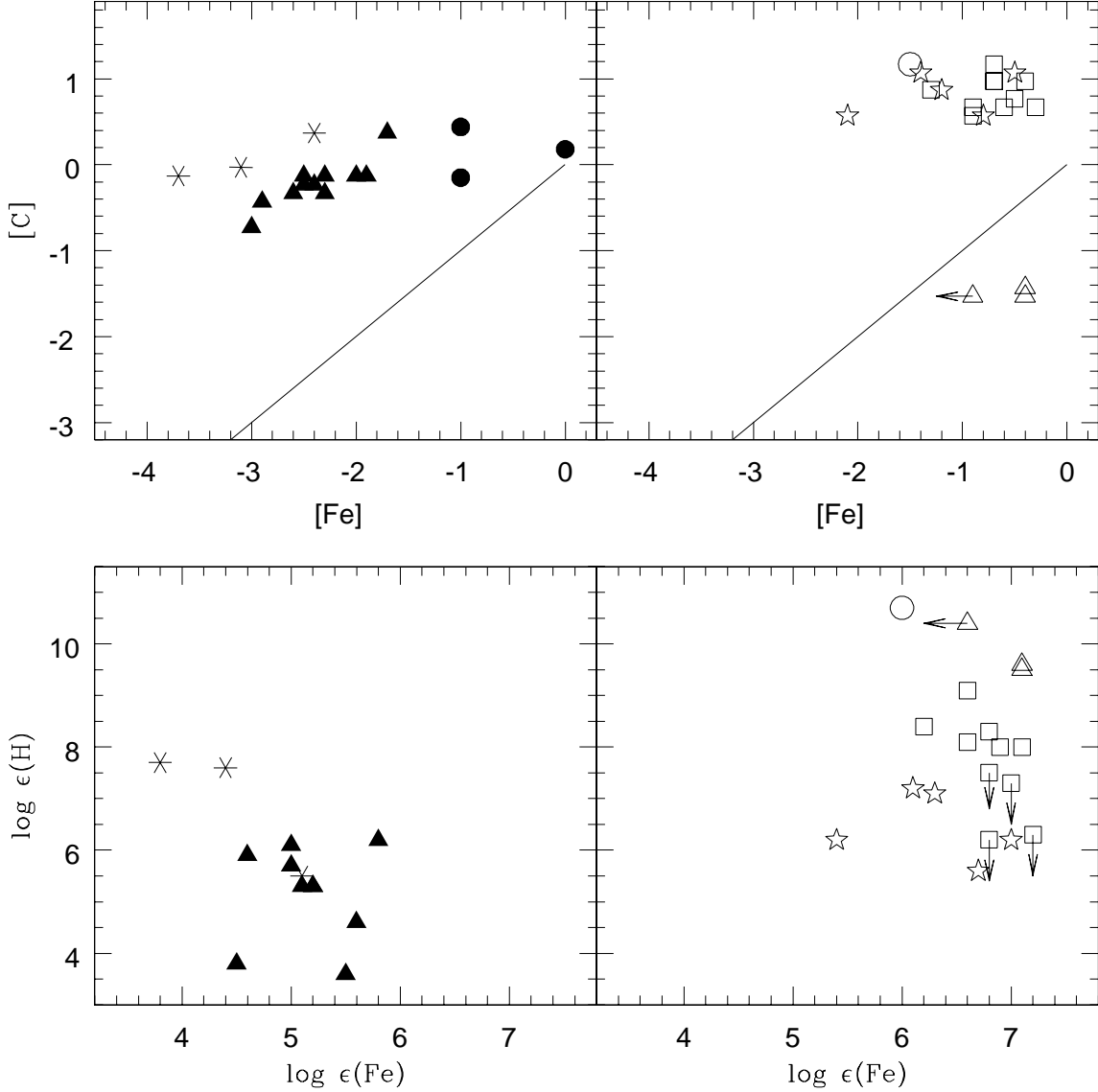


Fig. 1.— $\log \epsilon(H)$ vs. $\log \epsilon(Fe)$ for RCBs (bottom left panel) and EHes (bottom right panel). $[C]$ vs. $[Fe]$ for RCBs (top left panel) and EHes (top right panel). The majority and minority class RCBs are represented by filled triangles and asterisks, respectively. The hot and cool EHes are represented by open squares and open stars, respectively. C-poor EHes are represented by open triangles. DY Cen is represented by open circle. Filled circles denote the model predictions from Crawford et al. (2020) for three Model IDs SOL8.57, SUB8.48, and SUB8.53, meeting the maximum criteria; details are in the text of Section 6. $[C]=[Fe]$ is denoted by solid line, and $[Fe],[C]=0,0$ represents the Sun.

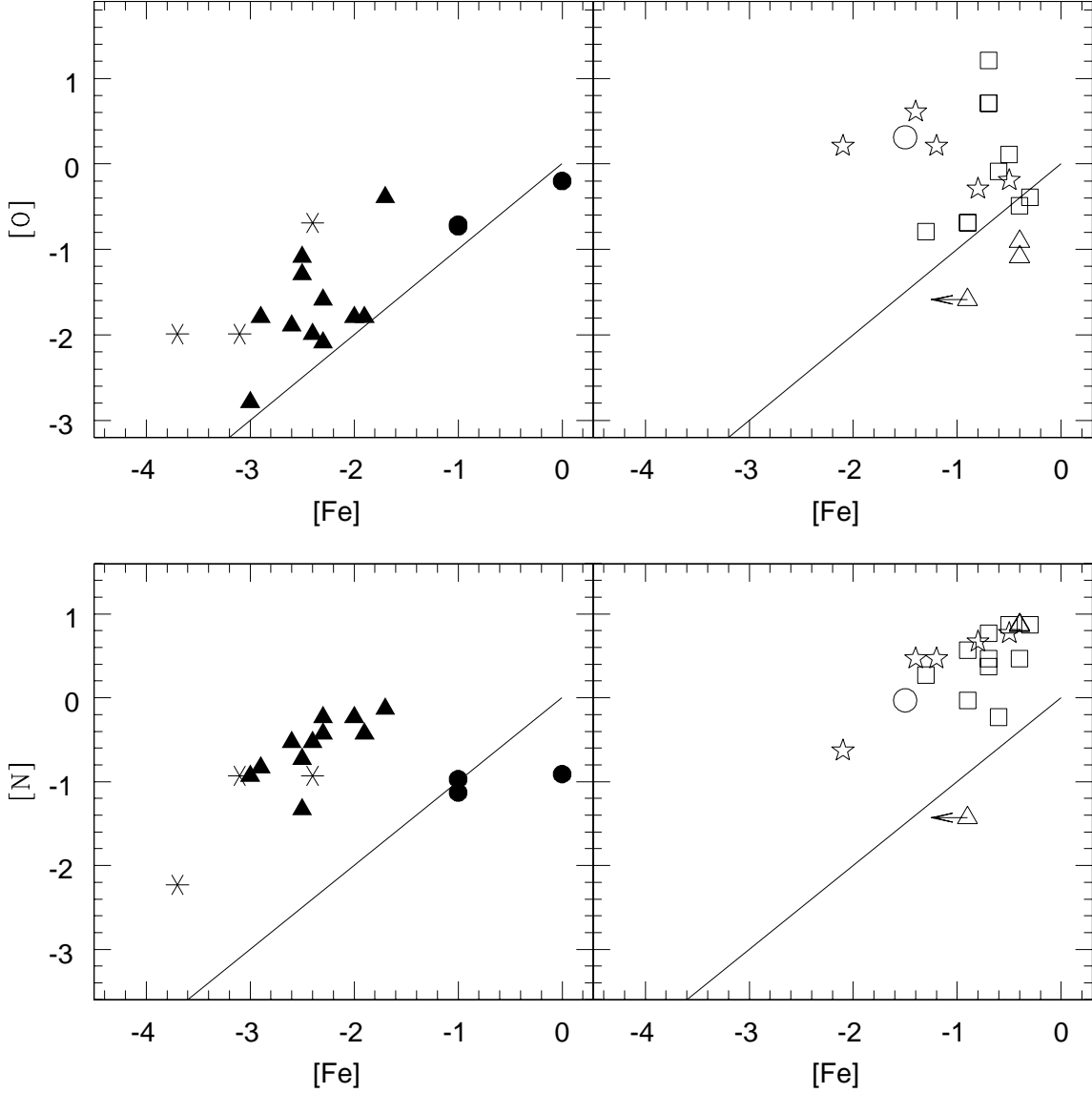


Fig. 2.— $[N]$ vs. $[Fe]$ for RCBs (bottom left panel) and EHes (bottom right panel). $[O]$ vs. $[Fe]$ for RCBs (top left panel) and EHes (top right panel). The majority and minority class RCBs are represented by filled triangles and asterisks, respectively. The hot and cool EHes are represented by open squares and open stars, respectively. C-poor EHes are represented by open triangles. DY Cen is represented by open circle. Filled circles denote the model predictions from Crawford et al. (2020) for three Model IDs SOL8.57, SUB8.48, and SUB8.53, meeting the maximum criteria; details are in the text of Section 6. $[X]=[Fe]$ are denoted by solid lines, where X represents N, and O. $[Fe],[X]=0,0$ represents the Sun.

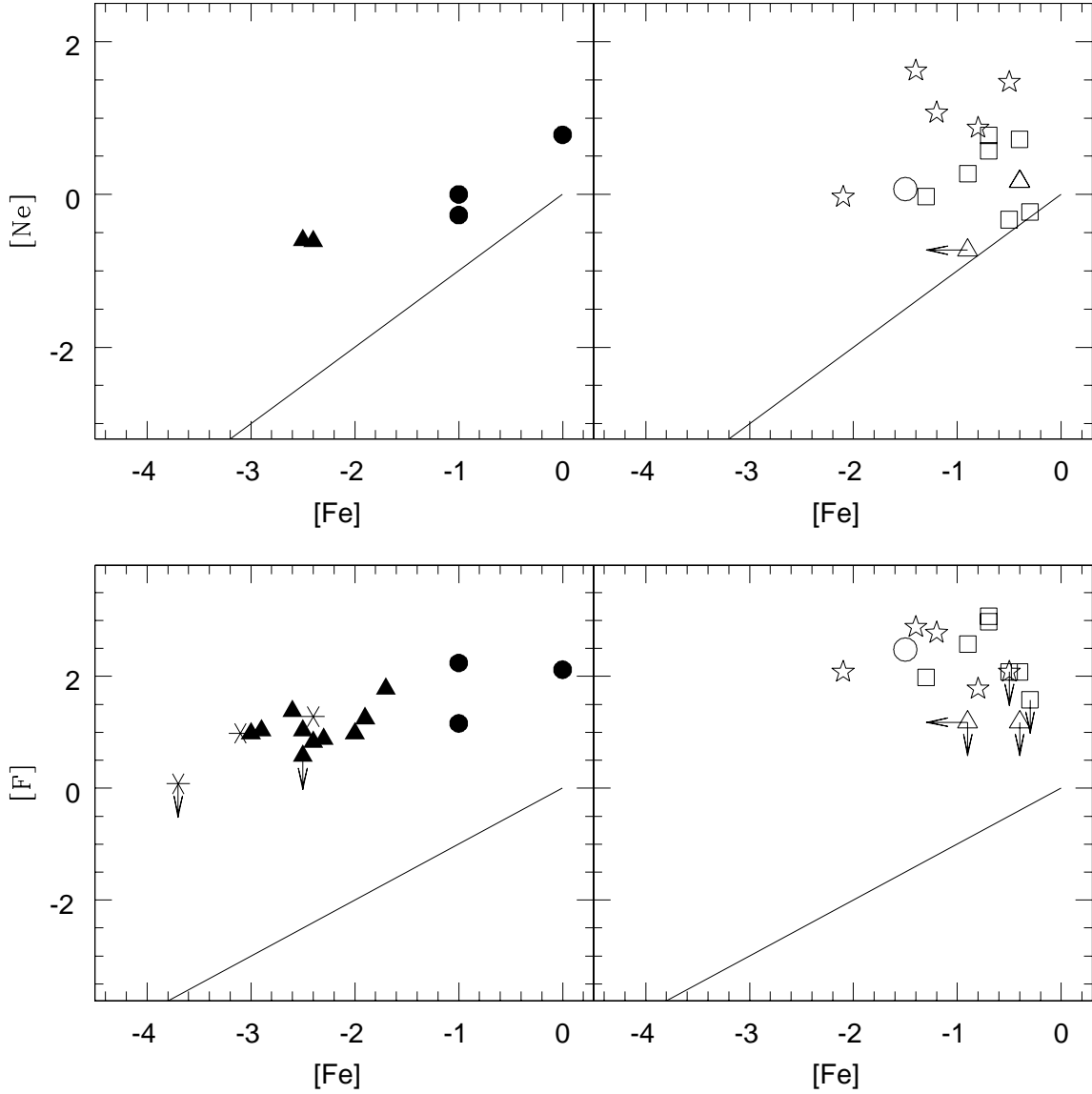


Fig. 3.— $[\text{F}]$ vs. $[\text{Fe}]$ for RCBs (bottom left panel) and EHes (bottom right panel). $[\text{Ne}]$ vs. $[\text{Fe}]$ for RCBs (top left panel) and EHes (top right panel). The majority and minority class RCBs are represented by filled triangles and asterisks, respectively. The hot and cool EHes are represented by open squares and open stars, respectively. C-poor EHes are represented by open triangles. DY Cen is represented by open circle. Filled circles denote the model predictions from Crawford et al. (2020) for three Model IDs SOL8.57, SUB8.48, and SUB8.53, meeting the maximum criteria; details are in the text of Section 6. $[\text{X}]=[\text{Fe}]$ are denoted by solid lines, where X represents F, and Ne. $[\text{Fe}],[\text{X}]=0,0$ represents the Sun.

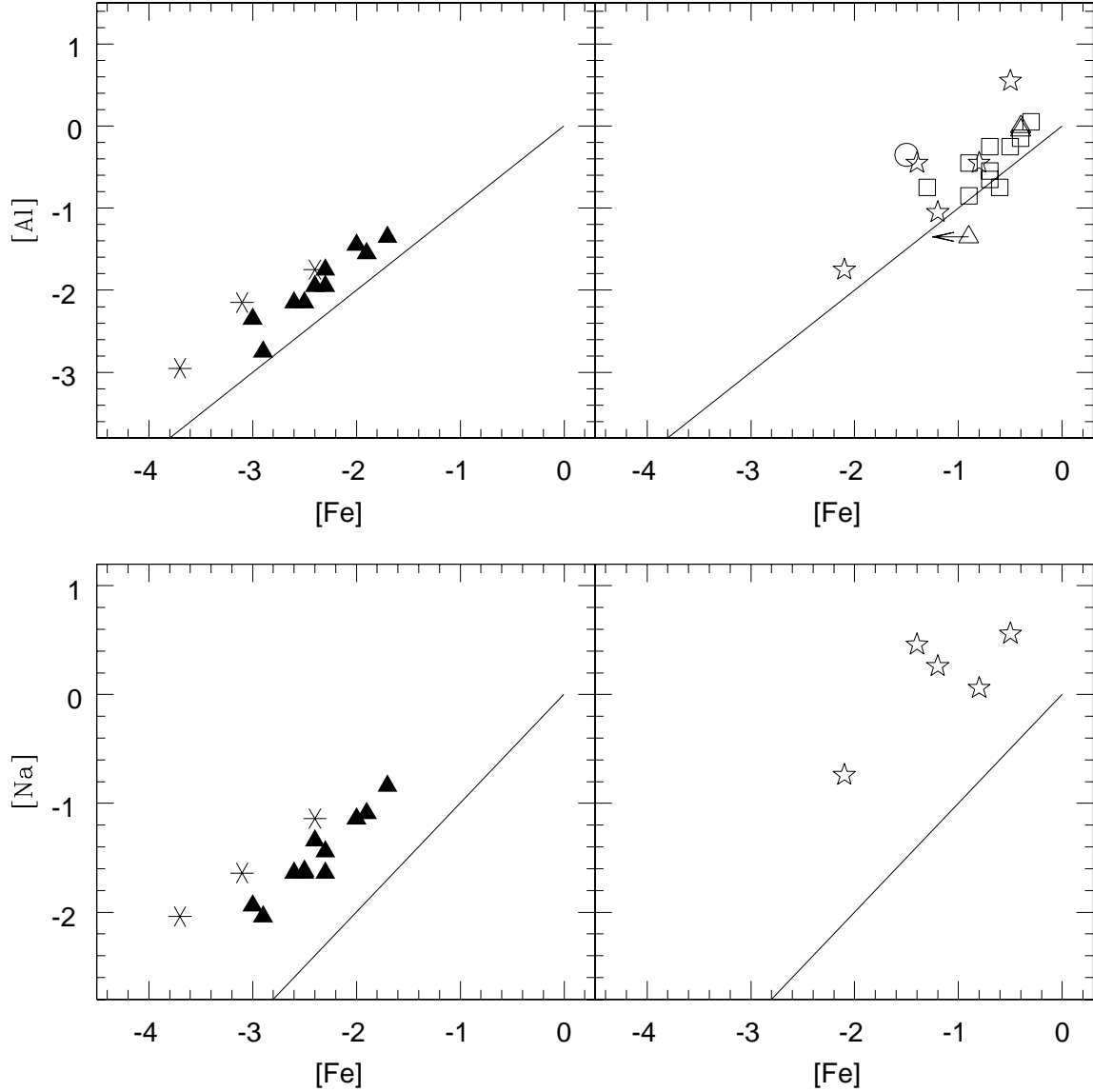


Fig. 4.— [Na] vs. [Fe] for RCBs (bottom left panel) and EHes (bottom right panel). [Al] vs. [Fe] for RCBs (top left panel) and EHes (top right panel). The majority and minority class RCBs are represented by filled triangles and asterisks, respectively. The hot and cool EHes are represented by open squares and open stars, respectively. C-poor EHes are represented by open triangles. DY Cen is represented by open circle. $[X]=[Fe]$ are denoted by solid lines, where X represents Na, and Al. $[Fe],[X]=0,0$ represents the Sun.

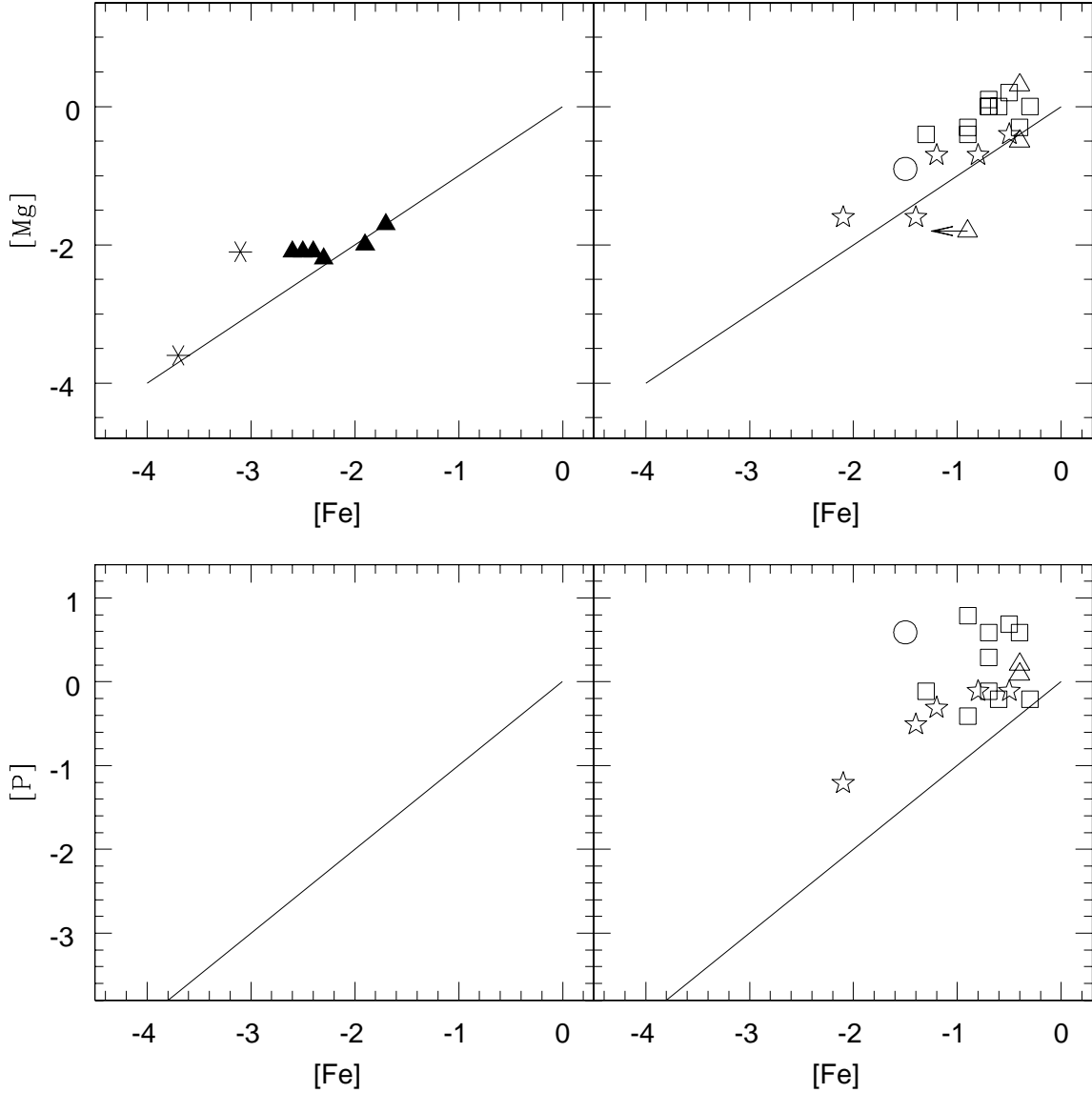


Fig. 5.— [P] vs. [Fe] for RCBs (bottom left panel) and EHes (bottom right panel). [Mg] vs. [Fe] for RCBs (top left panel) and EHes (top right panel). The majority and minority class RCBs are represented by filled triangles and asterisks, respectively. The hot and cool EHes are represented by open squares and open stars, respectively. C-poor EHes are represented by open triangles. DY Cen is represented by open circle. $[X]=[Fe]$ are denoted by solid lines, where X represents P, and Mg. $[Fe],[X]=0,0$ represents the Sun.

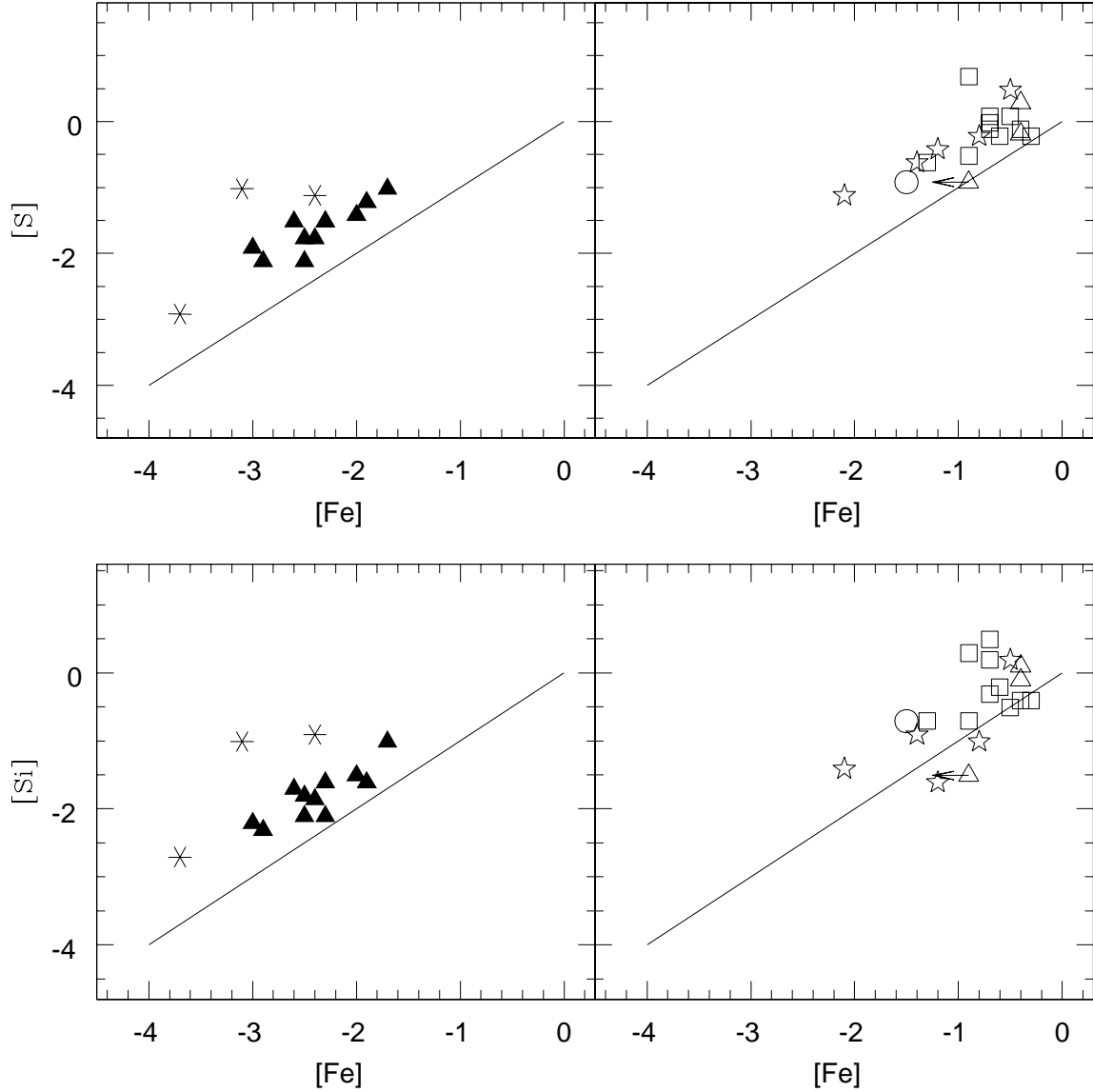


Fig. 6.— $[Si]$ vs. $[Fe]$ for RCBs (bottom left panel) and EHes (bottom right panel). $[S]$ vs. $[Fe]$ for RCBs (top left panel) and EHes (top right panel). The majority and minority class RCBs are represented by filled triangles and asterisks, respectively. The hot and cool EHes are represented by open squares and open stars, respectively. C-poor EHes are represented by open triangles. DY Cen is represented by open circle. $[X]=[Fe]$ are denoted by solid lines, where X represents Si, and S. $[Fe],[X]=0,0$ represents the Sun.

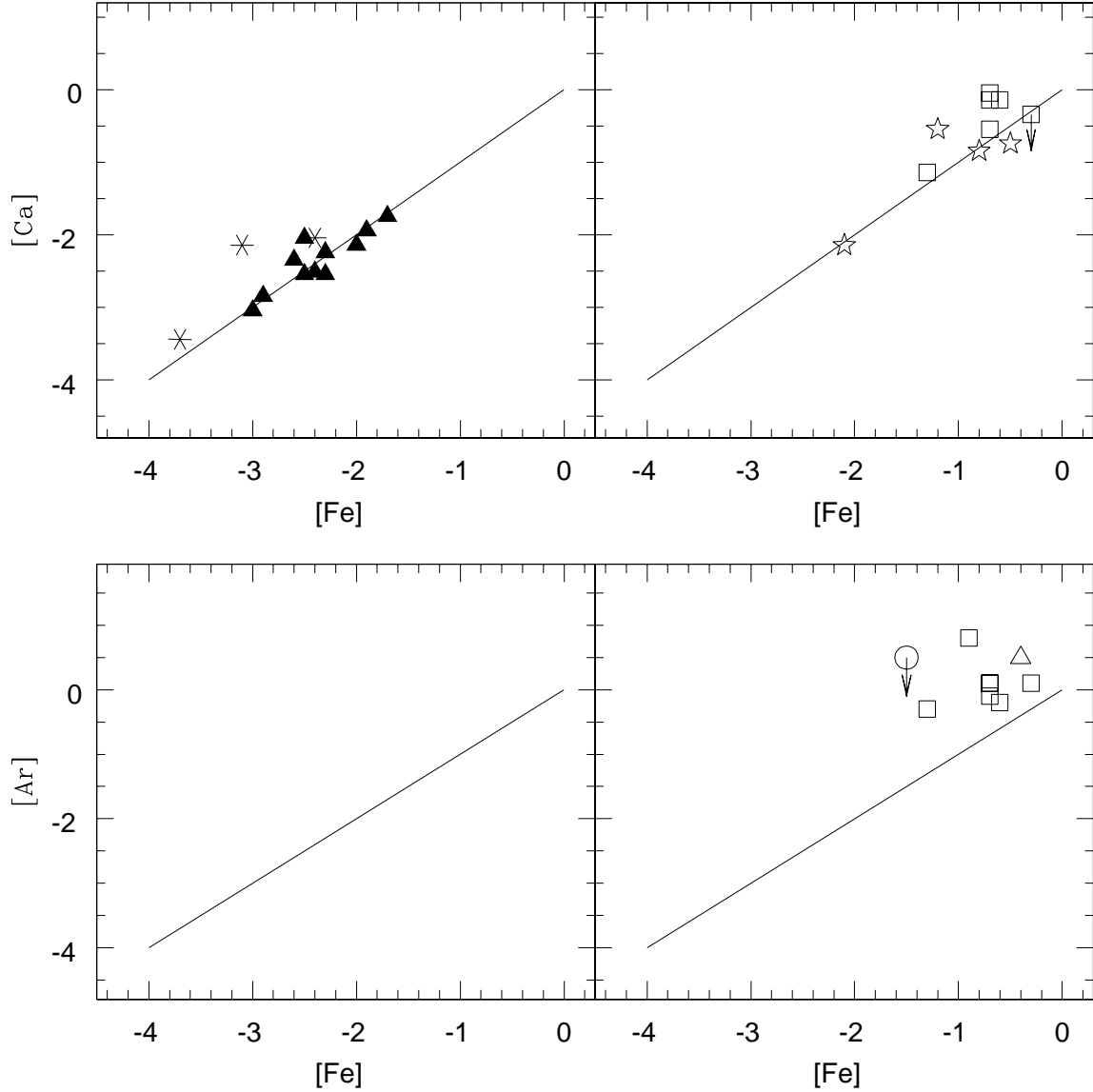


Fig. 7.— $[\text{Ar}]$ vs. $[\text{Fe}]$ for RCBs (bottom left panel) and EHes (bottom right panel). $[\text{Ca}]$ vs. $[\text{Fe}]$ for RCBs (top left panel) and EHes (top right panel). The majority and minority class RCBs are represented by filled triangles and asterisks, respectively. The hot and cool EHes are represented by open squares and open stars, respectively. C-poor EHes are represented by open triangles. DY Cen is represented by open circle. $[\text{X}]=[\text{Fe}]$ are denoted by solid lines, where X represents Ar, and Ca. $[\text{Fe}], [\text{X}]=0,0$ represents the Sun.

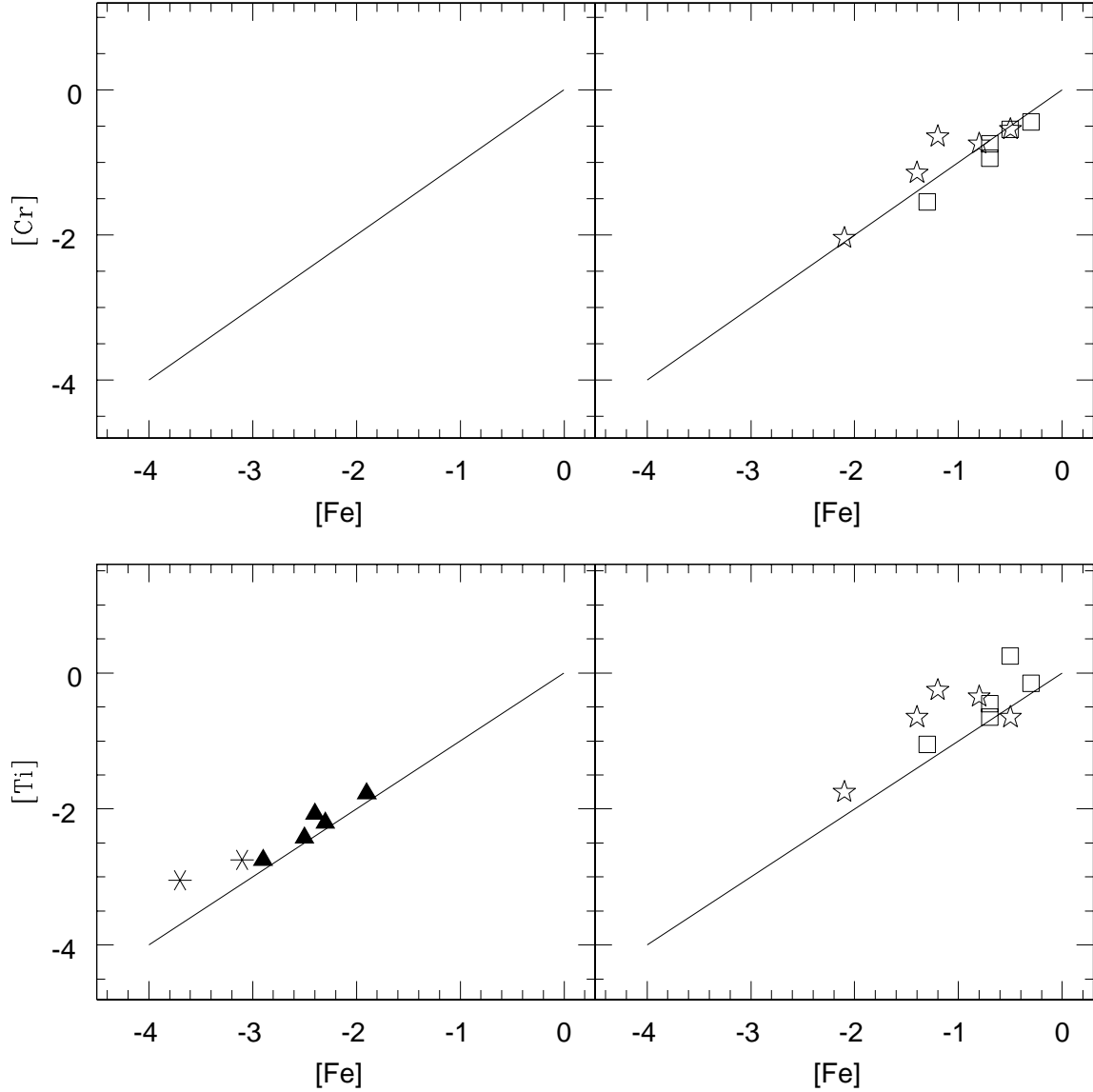


Fig. 8.— [Ti] vs. [Fe] for RCBs (bottom left panel) and EHes (bottom right panel). [Cr] vs. [Fe] for RCBs (top left panel) and EHes (top right panel). The majority and minority class RCBs are represented by filled triangles and asterisks, respectively. The hot and cool EHes are represented by open squares and open stars, respectively. $[X]=[Fe]$ are denoted by solid lines, where X represents Ti, and Cr. $[Fe],[X]=0,0$ represents the Sun.

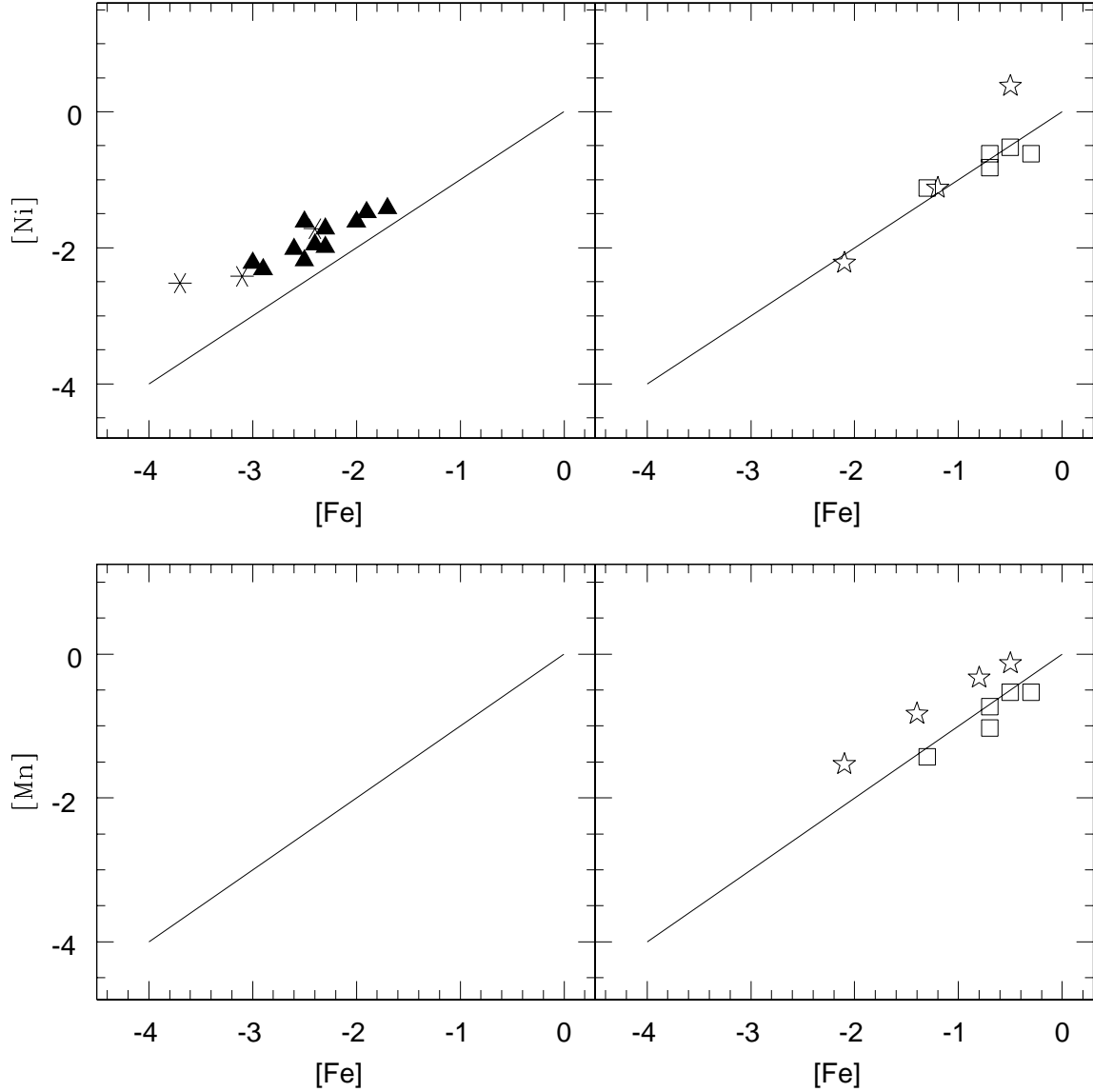


Fig. 9.— [Mn] vs. [Fe] for RCBs (bottom left panel) and EHes (bottom right panel). [Ni] vs. [Fe] for RCBs (top left panel) and EHes (top right panel). The majority and minority class RCBs are represented by filled triangles and asterisks, respectively. The hot and cool EHes are represented by open squares and open stars, respectively. $[X]=[Fe]$ are denoted by solid lines, where X represents Mn, and Ni. $[Fe],[X]=0,0$ represents the Sun.

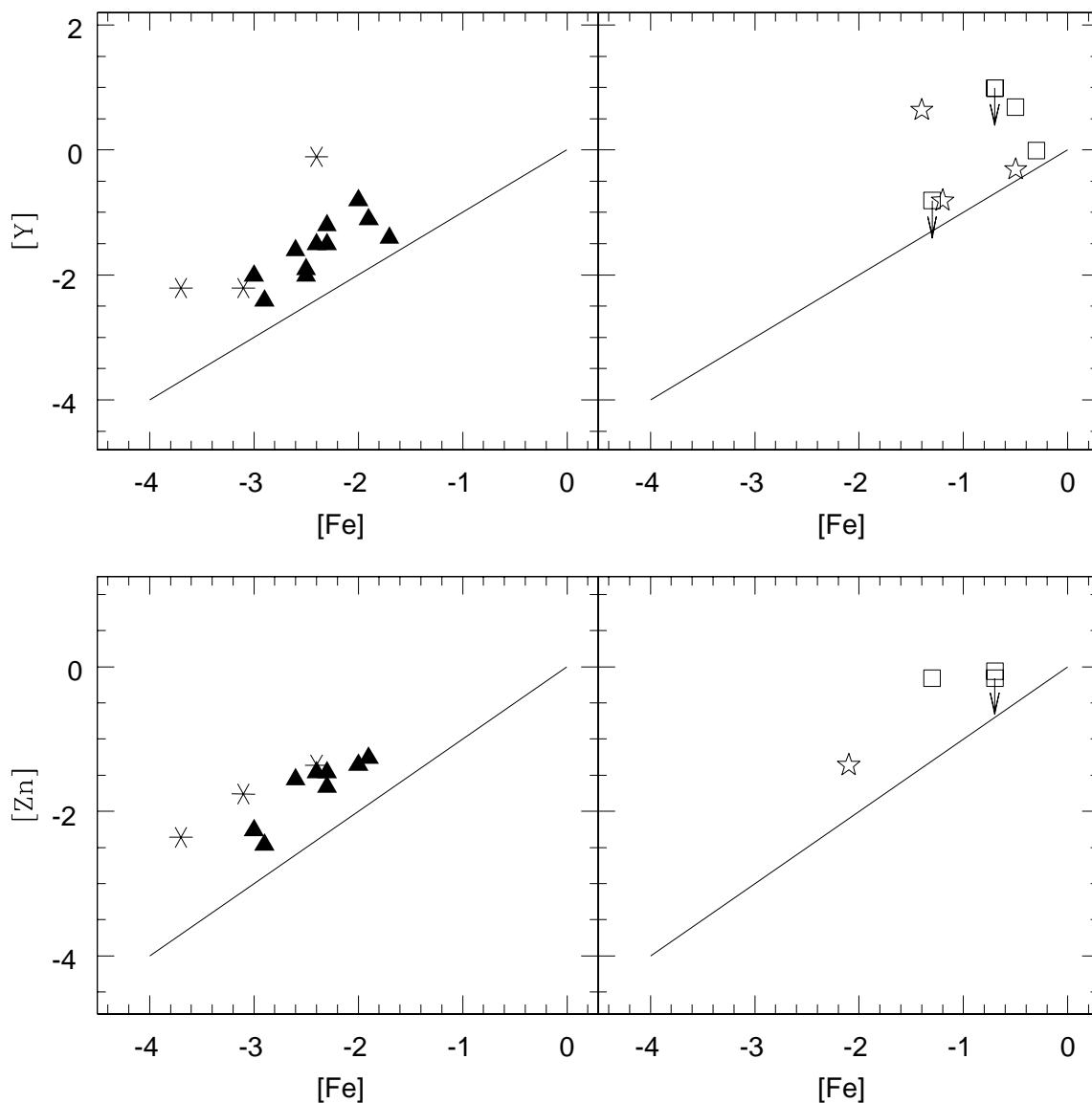


Fig. 10.— $[Zn]$ vs. $[Fe]$ for RCBs (bottom left panel) and EHes (bottom right panel). $[Y]$ vs. $[Fe]$ for RCBs (top left panel) and EHes (top right panel). The majority and minority class RCBs are represented by filled triangles and asterisks, respectively. The hot and cool EHes are represented by open squares and open stars, respectively. $[X]=[Fe]$ are denoted by solid lines, where X represents Zn, and Y. $[Fe],[X]=0,0$ represents the Sun.

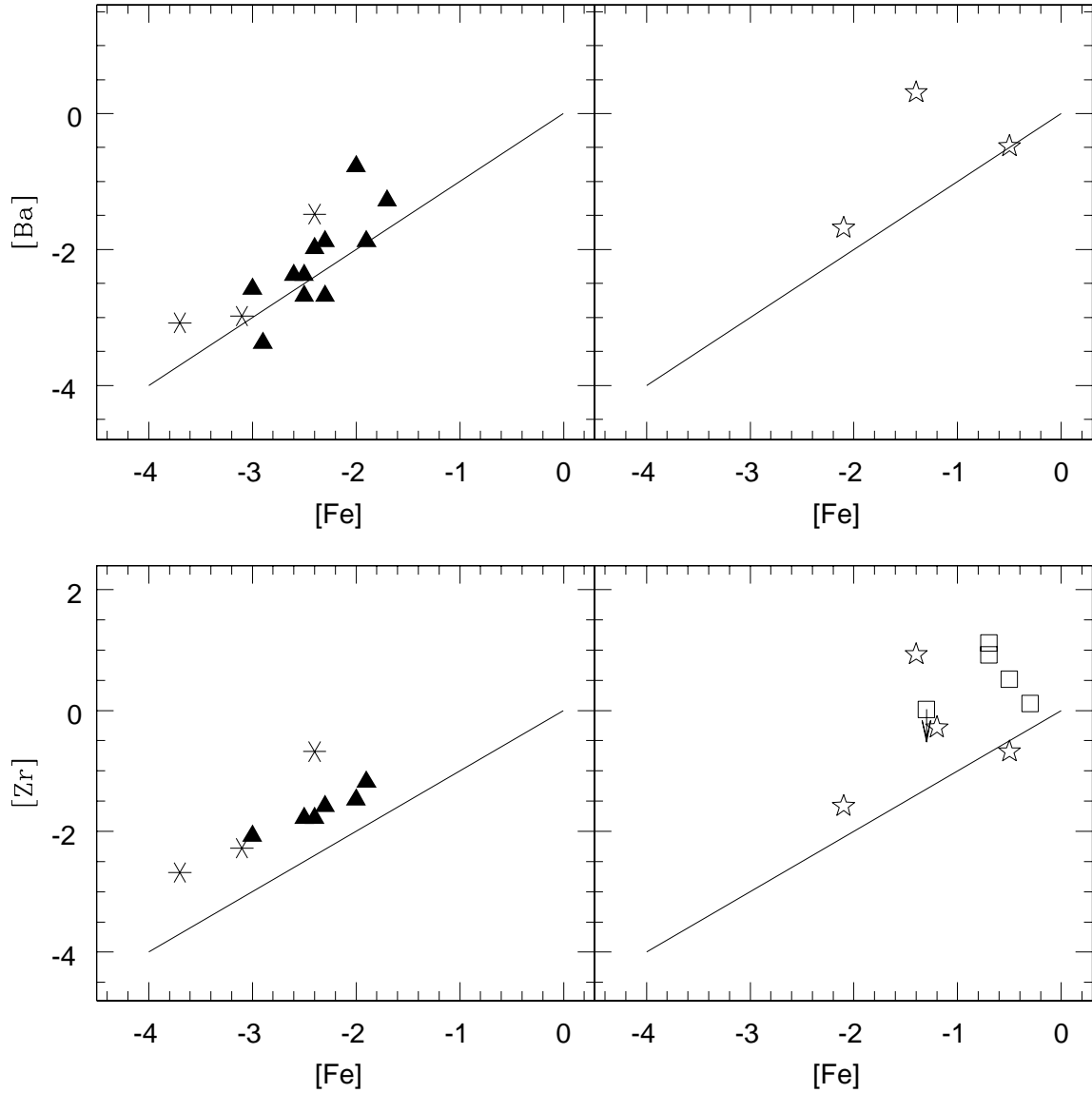


Fig. 11.— [Zr] vs. [Fe] for RCBs (bottom left panel) and EHes (bottom right panel). [Ba] vs. [Fe] for RCBs (top left panel) and EHes (top right panel). The majority and minority class RCBs are represented by filled triangles and asterisks, respectively. The hot and cool EHes are represented by open squares and open stars, respectively. $[X]=[Fe]$ are denoted by solid lines, where X represents Zr, and Ba. $[Fe],[X]=0,0$ represents the Sun.

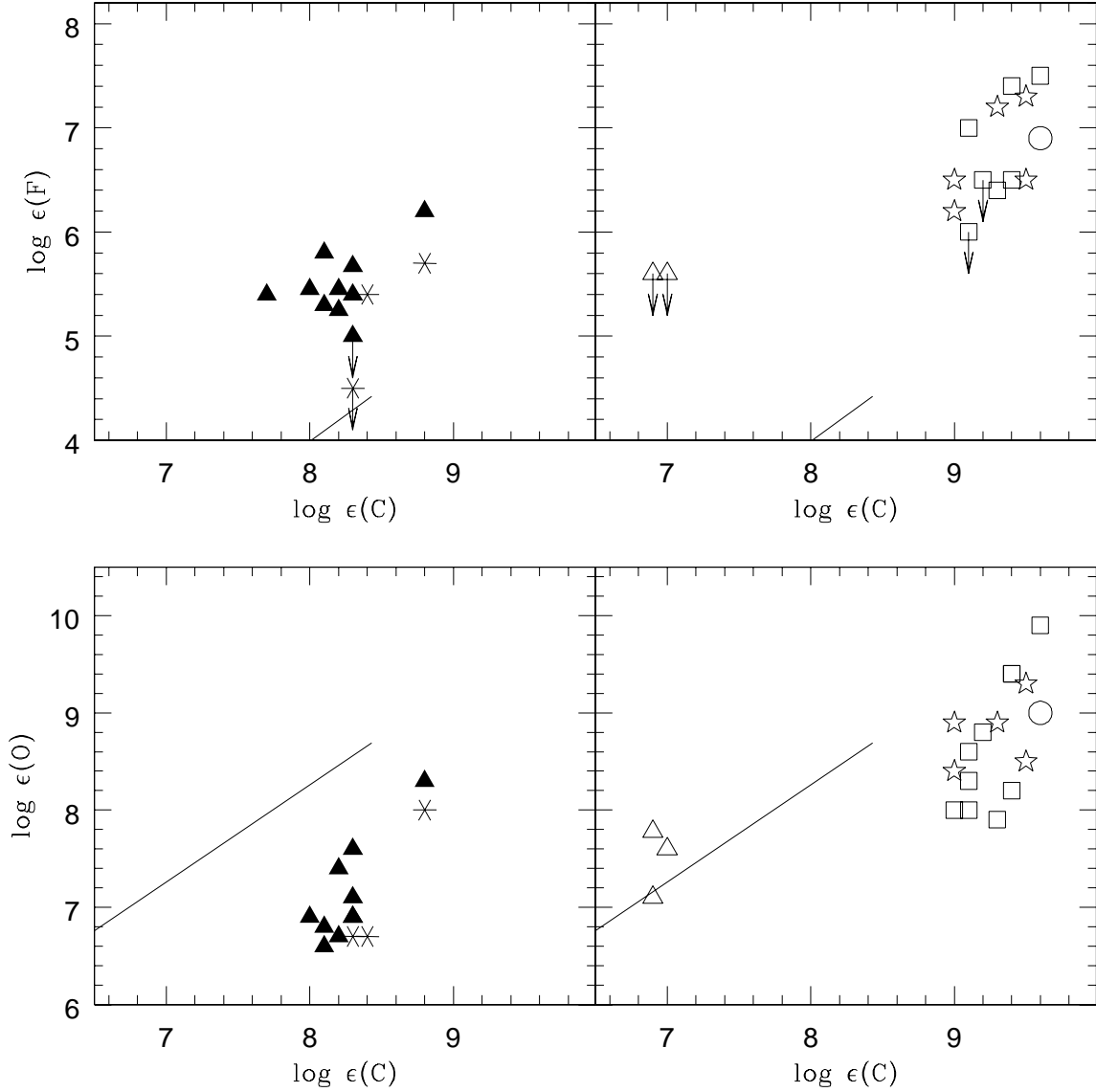


Fig. 12.— $\log \epsilon(O)$ vs. $\log \epsilon(C)$ for RCBs (bottom left panel) and EHes (bottom right panel). $\log \epsilon(F)$ vs. $\log \epsilon(C)$ for RCBs (top left panel) and EHes (top right panel). The majority and minority class RCBs are represented by filled triangles and asterisks, respectively. The hot and cool EHes are represented by open squares and open stars, respectively. C-poor EHes are represented by open triangles. DY Cen is represented by open circle. The solid lines denote the locus of the solar X/C ratios, where X represents O, and F.

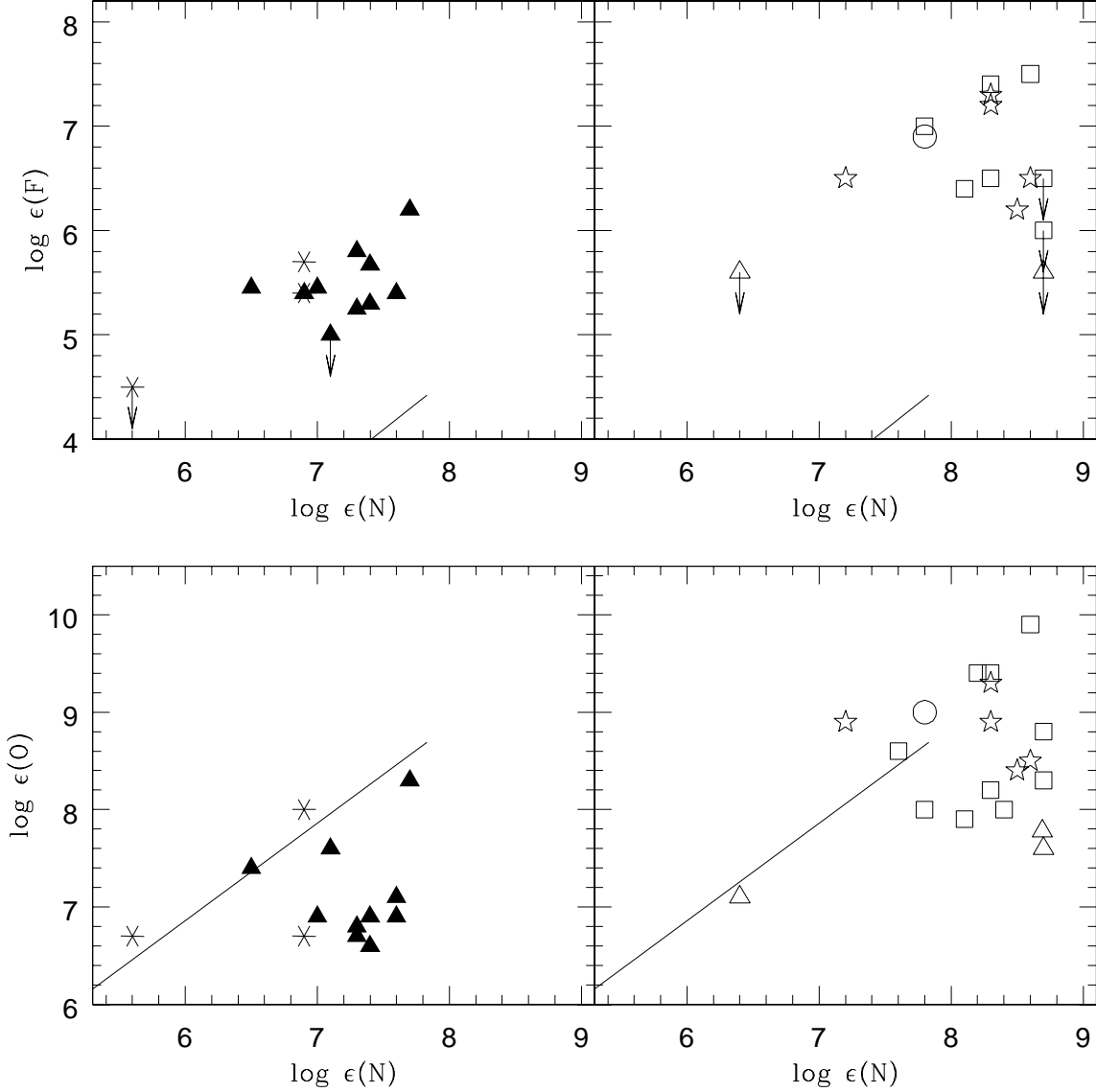


Fig. 13.— $\log \epsilon(O)$ vs. $\log \epsilon(N)$ for RCBs (bottom left panel) and EHes (bottom right panel). $\log \epsilon(F)$ vs. $\log \epsilon(N)$ for RCBs (top left panel) and EHes (top right panel). The majority and minority class RCBs are represented by filled triangles and asterisks, respectively. The hot and cool EHes are represented by open squares and open stars, respectively. C-poor EHes are represented by open triangles. DY Cen is represented by open circle. The solid lines denote the locus of the solar X/N ratios, where X represents O, and F.

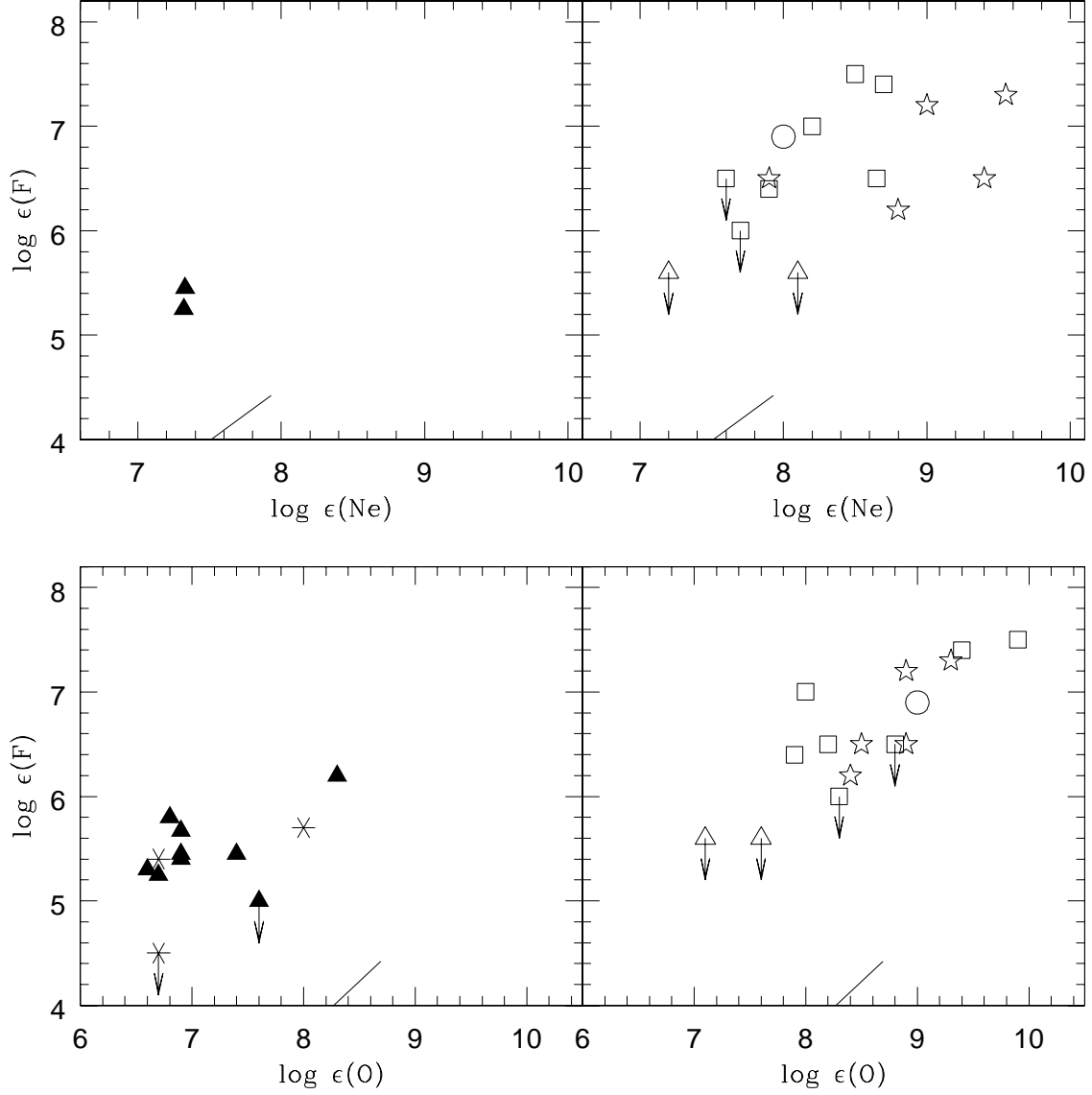


Fig. 14.— $\log \epsilon(\text{F})$ vs. $\log \epsilon(\text{O})$ for RCBs (bottom left panel) and EHes (bottom right panel). $\log \epsilon(\text{F})$ vs. $\log \epsilon(\text{Ne})$ for RCBs (top left panel) and EHes (top right panel). The majority and minority class RCBs are represented by filled triangles and asterisks, respectively. The hot and cool EHes are represented by open squares and open stars, respectively. C-poor EHes are represented by open triangles. DY Cen is represented by open circle. The solid lines denote the locus of the solar F/X ratios, where X represents O, and Ne.

Table 1. Revised photospheric abundances of RCBs

Element	GU Sgr	UX Ant	RCrB	RS Tel	SU Tau	V482 Cyg	FH Sct	V2552 Oph	V532 Oph	RCB8 ^a	RCB10 ^b	VZ Sgr	V CrA	V854 Cen	FF ^c	Sun ^d
H	...	5.7	6.2	5.3	5.9	3.6	3.8	5.3	5.3	4.6	6.1	5.5	7.6	7.7	8.2	12.0
Li	≤ -0.3	≤ 1.3	2.1	≤ 0.2	1.1	≤ -0.1	≤ -0.8	≤ -0.4	≤ -0.3	≤ -0.2	...	≤ 0.8	≤ -0.2	≤ -0.2	3.4	1.05
C	8.1	8.3	8.8	8.3	8.0	8.3	7.7	8.1	8.2	8.3	8.2	8.8	8.4	8.3	9.7	8.43
ΔC^e	1.4	1.2	0.7	1.2	1.5	1.2	1.8	1.4	1.3	1.2	1.3	0.7	1.1	1.2	0.8	...
N	7.3	7.1	7.7	7.6	7.0	7.6	6.9	7.4	7.3	7.4	6.5	6.9	6.9	5.6	8.1	7.83
O	6.8	7.6	8.3	7.1	6.9	6.9	5.9	6.6	6.7	6.9	7.4	8.0	6.7	6.7	8.6	8.69
F	5.8	5.0	6.2	...	5.5	5.4	5.4	5.3	5.3	5.7	5.5	5.7	5.4	4.5	<5.6	4.42
Ne	7.3	...	7.3	7.93
Na	4.6	4.6	5.4	4.8	4.2	5.1	4.3	4.6	4.9	5.2	4.6	5.1	4.6	4.2	6.0	6.24
Mg	5.5	...	5.9	5.4	5.5	5.6	5.5	...	5.5	4.0	5.7	7.60
Al	4.3	...	5.1	4.7	3.7	5.0	4.1	4.5	4.5	4.9	4.3	4.7	4.3	3.5	5.5	6.45
Si	5.8	5.7	6.5	5.9	5.2	6.0	5.3	5.4	5.7	5.9	5.4	6.6	6.5	4.8	6.7	7.51
P	5.41
S	5.6	5.0	6.1	5.6	5.0	5.7	5.2	5.6	5.4	5.9	5.4	6.0	6.1	4.2	6.1	7.12
Ca	4.0	4.3	4.6	4.1	3.5	4.2	3.3	3.8	3.8	4.4	3.8	4.3	4.2	2.9	4.7	6.34
Ti	2.2	2.8	2.9	3.2	2.5	...	2.2	1.9	3.8	4.95
Fe	4.9	5.0	5.8	5.2	4.6	5.5	4.5	5.2	5.1	5.6	5.0	5.1	4.4	3.8	5.8	7.50
Ni	4.2	4.6	4.8	4.5	3.9	4.6	4.0	4.2	4.3	4.7	4.0	4.5	3.8	3.7	5.4	6.22
Zn	3.0	3.1	2.1	3.2	2.3	2.9	3.1	3.3	...	3.2	2.8	2.2	4.6	4.56
Y	0.6	0.3	0.8	0.7	-0.2	1.4	0.2	1.0	0.7	1.1	0.2	2.1	3.4	2.21
Zr	1.1	0.5	1.0	0.8	1.4	0.8	1.9	0.3	-0.1	2.7	2.58
Ba	-0.2	-0.2	0.9	0.3	-1.2	1.4	-0.4	-0.5	0.2	0.3	-0.5	0.7	-0.8	-0.9	1.1	2.18

^aASAS-RCB-8

^bASAS-RCB-10

^cV4334 Sgr (Sakurai's object), a FF product, shows no detectable neutral fluorine lines (Pandey et al. 2008)

^dAsplund et al. (2009)

^e $\Delta C = C(\text{assumed for the model}) - C(\text{derived from } C_2 \text{ bands})$. For the RCB stars assumed $C/He=1\%$ or $C=9.5$ dex, and for FF object assumed $C/He=10\%$ or $C=10.5$ dex.

REFERENCES

- Asplund, M., Grevesse, N., Sauval, A. J., & Scott, P. 2009, *ARA&A*, 47, 481
- Asplund, M., Gustafsson, B., Kiselman, D., & Eriksson, K. 1997a, *A&A*, 318, 521
- Asplund, M., Gustafsson, B., Lambert, D. L., & Kameswara Rao, N. 1997b, *A&A*, 321, L17
- Asplund, M., Gustafsson, B., Lambert, D. L., & Rao, N. K. 2000, *A&A*, 353, 287
- Bhowmick, A., Pandey, G., & Lambert, D. L. 2020, *ApJ*, 891, 40
- Clayton, G. C., Geballe, T. R., Herwig, F., Fryer, C., & Asplund, M. 2007, *ApJ*, 662, 1220
- Crawford, C. L., Clayton, G. C., Munson, B., Chatzopoulos, E., & Frank, J. 2020, *MNRAS*, 498, 2912
- Dehnen, W., & Binney, J. J. 1998, *MNRAS*, 298, 387
- Drilling, J. S., Jeffery, C. S., & Heber, U. 1998, *A&A*, 329, 1019
- Flynn, C., Sommer-Larsen, J., & Christensen, P. R. 1996, *MNRAS*, 281, 1027
- Gaia Collaboration et al. 2016, *A&A*, 595, A2
- . 2020, *A&A*, 642, C1
- Hema, B., Pandey, G., & Lambert, D. L. 2012a, in *Nuclei in the Cosmos (NIC XII)*, ed. J. Lattanzio, A. Karakas, M. Lugaro, & G. Dracoulis, 195
- Hema, B. P., Pandey, G., Kamath, D., Kameswara Rao, N., Lambert, D., & Woolf, V. M. 2017, *PASP*, 129, 104202
- Hema, B. P., Pandey, G., & Lambert, D. L. 2012b, *ApJ*, 747, 102
- Herwig, F. 2001, *Ap&SS*, 275, 15
- Howes, L. M., et al. 2015, *Nature*, 527, 484
- Iben, Jr., I., Kaler, J. B., Truran, J. W., & Renzini, A. 1983, *ApJ*, 264, 605
- Iben, Jr., I., & Tutukov, A. V. 1984, *ApJS*, 54, 335
- Jeffery, C. S. 1998, *MNRAS*, 294, 391
- . 2017, *MNRAS*, 470, 3557

- Jeffery, C. S., Drilling, J. S., & Heber, U. 1987, MNRAS, 226, 317
- Jeffery, C. S., Hamill, P. J., Harrison, P. M., & Jeffers, S. V. 1998, A&A, 340, 476
- Jeffery, C. S., & Heber, U. 1992, A&A, 260, 133
- Jeffery, C. S., Heber, U., Hill, P. W., & Pollacco, D. 1988, MNRAS, 231, 175
- Jeffery, C. S., Rao, N. K., & Lambert, D. L. 2020, MNRAS, 493, 3565
- Johnson, D. R. H., & Soderblom, D. R. 1987, AJ, 93, 864
- Karambelkar, V. R., et al. 2021, ApJ, 910, 132
- Kerr, F. J., & Lynden-Bell, D. 1986, MNRAS, 221, 1023
- Lauer, A., Chatzopoulos, E., Clayton, G. C., Frank, J., & Marcello, D. C. 2019, MNRAS, 488, 438
- Longland, R., Lorén-Aguilar, P., José, J., García-Berro, E., Althaus, L. G., & Isern, J. 2011, ApJ, 737, L34
- Menon, A., Herwig, F., Denissenkov, P. A., Clayton, G. C., Staff, J., Pignatari, M., & Paxton, B. 2013, ApJ, 772, 59
- Menon, A., Karakas, A. I., Lugaro, M., Doherty, C. L., & Ritter, C. 2019, MNRAS, 482, 2320
- Munson, B., Chatzopoulos, E., Frank, J., Clayton, G. C., Crawford, C. L., Denissenkov, P. A., & Herwig, F. 2021, ApJ, 911, 103
- Pandey, G. 2006, ApJ, 648, L143
- Pandey, G., Kameswara Rao, N., Jeffery, C. S., & Lambert, D. L. 2014, ApJ, 793, 76
- Pandey, G., Kameswara Rao, N., & Lambert, D. L. 1996, MNRAS, 282, 889
- Pandey, G., Kameswara Rao, N., Lambert, D. L., Jeffery, C. S., & Asplund, M. 2001, MNRAS, 324, 937
- Pandey, G., & Lambert, D. L. 2011, ApJ, 727, 122
- . 2017, ApJ, 847, 127
- Pandey, G., Lambert, D. L., Jeffery, C. S., & Rao, N. K. 2006, ApJ, 638, 454

- Pandey, G., Lambert, D. L., & Rao, N. K. 2008, *ApJ*, 674, 1068
- Pandey, G., Lambert, D. L., Rao, N. K., Gustafsson, B., Ryde, N., & Yong, D. 2004a, *MNRAS*, 353, 143
- Pandey, G., Lambert, D. L., Rao, N. K., & Jeffery, C. S. 2004b, *ApJ*, 602, L113
- Pandey, G., & Reddy, B. E. 2006, *MNRAS*, 369, 1677
- Rao, N. K., & Lambert, D. L. 1996, in *Astronomical Society of the Pacific Conference Series*, Vol. 96, *Hydrogen Deficient Stars*, ed. C. S. Jeffery & U. Heber, 43–+
- Rao, N. K., & Lambert, D. L. 2008, *MNRAS*, 384, 477
- Reddy, A. B. S., Lambert, D. L., & Giridhar, S. 2016, *MNRAS*, 463, 4366
- Tisserand, P., et al. 2020, *A&A*, 635, A14
- Webbink, R. F. 1984, *ApJ*, 277, 355
- Wu, Z.-Y., Zhou, X., Ma, J., & Du, C.-H. 2009, *MNRAS*, 399, 2146
- Zhang, X., & Jeffery, C. S. 2012a, *MNRAS*, 426, L81
- . 2012b, *MNRAS*, 419, 452
- Zhang, X., Jeffery, C. S., Chen, X., & Han, Z. 2014, *MNRAS*, 445, 660